Chemical Science

ROYAL SOCIETY OF CHEMISTRY

EDGE ARTICLE

View Article Online
View Journal | View Issue

Cite this: *Chem. Sci.*, 2024, **15**, 9657

All publication charges for this article have been paid for by the Royal Society of Chemistry

Enhancing corannulene chemiluminescence, electrochemiluminescence and photoluminescence by means of an azabora-helicene to slow down its bowl inversion†

Xiaoli Qin, ‡[ab] Lin Huang, ‡[cde] Ziying Zhan,‡[a] Peng Fu,[cde] Qing Wang,[cf] Congyang Zhang,[a] Jianhui Huang *[cde] and Zhifeng Ding *[a]

Aromatic system extension of corannulene (**Cor**) is a synthetic challenge to access non-planar polyaromatic hydrocarbons (PAHs). Herein, we report the design and synthesis of azaborahelicene corannulene **1** through hybridization of an azabora[5] helical structure and subsequent luminescence studies. Significant enhancement in chemiluminescence (CL), electroluminescence (ECL) and photoluminescence (PL) is achieved compared to those of pristine **Cor**. Specifically, hybrid **1** shows a notable augmentation in absolute luminescence quantum efficiencies: 25-fold for CL, up to 23-fold for ECL with BPO as a coreactant, and 30-fold for PL, respectively, compared to those of pristine **Cor**. Intriguingly, the blue light emission observed in all three luminescence types suggests the presence of a single excited state. As revealed by variable-temperature (VT) ^{1}H NMR experiments, the bowl inversion frequency apparently decelerates by the steric effect of the helix motif in **1**, which could contribute to the enhanced luminescent properties by reducing excited energy losses non-radiatively through fewer molecular motions; these enhanced luminescence observations could be categorized alongside the aggregation induced emission (AIE) and crystallization-induced emission (CIE) phenomena. This work not only provides fundamental insights into improved luminescence quantum efficiencies *via* strategic modulation of the molecular structure and geometry, but the work also reveals **Cor**'s inherent potential to build efficient blue-light emitting materials and devices.

Received 5th March 2024
Accepted 3rd May 2024

DOI: 10.1039/d4sc01524j

rsc.li/chemical-science

1 Introduction

Corannulene (**Cor**), the smallest curved unit of C_{60}, is generally revered for its unique properties originating from the bowl-shaped structure; such properties include great intermolecular packing,[1–3] fast dynamic inversion behavior,[4–8] and specific electron deficiency,[9–11] in comparison to those of the classical planar graphene forms. Although the large π-surface of corannulene is comparable to that of pyrene, with an expectation of strong luminescence properties, **Cor** is in fact a relatively weak luminophore,[12–14] owing to the highly symmetric C_{5v} structure of corannulene, which also entails decreased quantum yields due to the Ham effect.[15] The bowl strain could also contribute to the diminished luminescence. Warner and co-workers hypothesized that **Cor**'s nonplanar strained ring structure might reduce oscillator strength and correspondingly the radiative rate constant.[16] Very recently, Zysman-Colman and Sigel *et al.* reported multiple phosphorescence by decorating corannulene with different donors.[17] Based on Tang and co-workers' pioneering studies on aggregation induced emission (AIE) and aggregation caused quenching (ACQ) of siloles as well as crystallization-induced emission phenomena,[18,19] the consensus is that free and fast inversion of the bowl molecule provides an opportune means by which excited energy is lost non-radiatively. A bright emission as radiative relaxation is anticipated through preventing this energy loss.

Our research interests have recently focused on the design and synthesis of a new curved aromatic system by elongating the corannulene π-system with a non-conventional C-centered scaffold. Specifically, we aim to introduce heteroatoms to

[a]*Department of Chemistry, Western University, London, ON N6A 5B7, Canada. E-mail: zfding@uwo.ca*

[b]*College of Chemistry and Material Science, Hunan Agricultural University, Changsha 410128, China*

[c]*School of Pharmaceutical Science and Technology, Faculty of Medicine, Tianjin University, Tianjin 300072, China. E-mail: jhuang@tju.edu.cn*

[d]*International Center of Chemical Science and Engineering, Tianjin 300072, China*

[e]*International Joint Research Centre for Molecular Sciences, Tianjin University, Tianjin 300072, China*

[f]*National Institute of Biological Sciences, No. 7 Science Park Road, Zhongguancun Life Science Park, Beijing 102206, China*

† Electronic supplementary information (ESI) available. CCDC 2337637. For ESI and crystallographic data in CIF or other electronic format see DOI: https://doi.org/10.1039/d4sc01524j

‡ X. Qin, L. Huang and Z. Zhan contributed equally to this work.

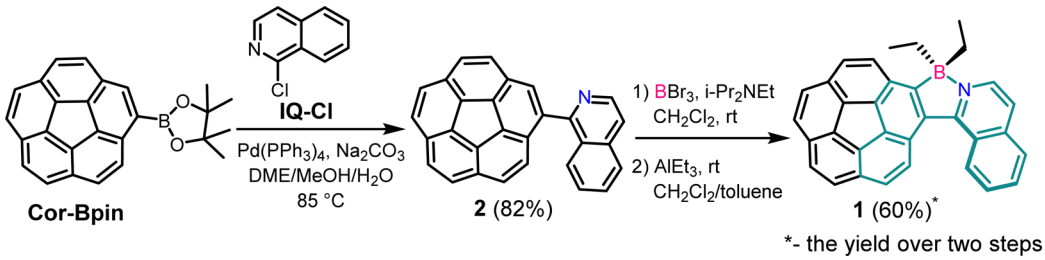

Scheme 1 Synthesis of organoboron corannulene–helicene compound **1** with the azaborahelicene motif highlighted in green.

modify electronic and steric effects to ultimately restrain intermolecular π–π stacking and molecular inversion. The incorporation of a boron (B) atom into π-conjugated scaffolds would provide **Cor** with high electron affinity[20] and carrier mobility,[21,22] generating potential for application in optoelectronic materials.[23,24] In the construction of coordinated organoboron compounds, the critical roles of B^{III} are (1) to stabilize the ligand by coordination and (2) to render the π system planar,[25] allowing intramolecular electron delocalization to intensify the emission and also the formation of rigid π-conjugated skeletons by reducing the lowest unoccupied molecular orbital (LUMO) energy level.[3,26] Although reported arylethynylated corannulenes have demonstrated increases in luminescence quantum yields,[3] boron-incorporated corannulenes are still scarcely explored. Furthermore, new B–N-doped aromatic compounds have been synthesized to have excellent optoelectronic properties.[27] Interestingly, helicenes that incorporate heteroatoms, such as azabora[5]helicene, along with its photophysical properties have been reported.[28] Herein, we report the construction of corannulene dialkyl borate **1** by employing isoquinoline as a chelating ligand (Scheme 1). The use of isoquinoline as a chelating ligand led to an azabora-helicene-corannulene hybrid structure, in which the steric repulsion of the helix structure potentially suppresses the inversion process of the bowl motif. Concurrently, the hybrid structure broke doubly degenerate LUMOs in **Cor**[29] by disrupting the C_{5v} symmetry, enhancing the overall luminescence.[3] Moreover, the presence of diethyl groups in azaborahelicene-**Cor 1** balances the Lewis acidity of the boron atom, thus increasing the **Cor** motif's electron density and lowering its oxidation potential, which facilitates chemiluminescence (CL), electrochemiluminescence (ECL) and photoluminescence (PL). Notably, the two ethyl groups provide excellent diastereotopic protons, accidently enabling a comprehensive exploration of the dynamic inversion behaviors of the bowl and helix motifs by variable-temperature (VT) NMR experiments, simultaneously.

Molecule **1** was observed to have greatly enhanced performances with respect to CL, ECL, and PL. These findings have promising implications for the development of luminescent materials based on curved aromatic hydrocarbons like **Cor**.

2 Results and discussion

2.1 Synthesis

Pinacol corannuleneboronate (**Cor-Bpin**) was synthesized according to the literature procedures.[30] Compound **2** was synthesized by Suzuki–Miyaura coupling of **Cor-Bpin** and commercially available 1-chloroisoquinoline (IQ-Cl) (ESI, Fig. S1 and S2†). In order to introduce a boron atom into intermediate **2**, we adapted the method reported by Murakami *et al.*[31] with some modifications. Briefly, in the presence of i-Pr_2NEt, compound **2** reacted with BBr_3 to give complex **1-Br$_2$** under an argon atmosphere. Our desired product, corannulene diethyl borate **1**, was successfully synthesized by the exchange of the bromide with the ethyl group under mild conditions with an overall yield of 60% (two steps) (Fig. S3–S5†). It turns out that protons in the ethyl group are very effective probes to determine inversion of corannulene and helicene.

2.2 X-ray crystallography

Slow evaporation of a dichloromethane solution furnished yellow block-like racemic crystals of **1**, which crystallized in the $P2_1/n$ space group, with a convex form as shown in Fig. 1 and S6.† The B–N bond length is 1.601 Å, indicating a strong B–N interaction, as shown in Fig. 1A and S6A.† While the parent **Cor** has a homogeneous depth of 0.87 Å,[32,33] bowl depth of **1** was found to vary. For instance, the perpendicular distance from the plane of the five-membered ring hub (C19–C23–C9–C39–C18 ring) to the parallel planes containing the carbon atoms C33 and C37 were found to be 0.81 Å and 0.68 Å, while the depth of the other rim carbon atoms to the bowl bottom was determined to be 0.91 Å on average (Fig. 1B). This asymmetric feature of bowl depths indicates that the steric effect of the helix motif could also affect the bowl structure of the **Cor** motif and change the bowl-to-bowl inversion process.[8] The steric repulsion of the helix motif in **1** is reflected to the longer rim C33═C37 bond (1.41 Å) than other rim C═C bonds (1.36–1.38 Å). The curvature of **1** is further evaluated by using Haddon's pi-orbital axis vector (POAV) angles.[34,35] As shown in Fig. 1A, the POAV angle around the central 5-membered ring is 8.2° equal to that of pristine **Cor**,[36] illustrating a similar curvature despite the slightly deformed bowl-structure of **1**. In comparison to four-coordinate organoboron analogues with isoquinolinyl and naphthyl motifs (dihedral angles: 16.8° and 27.7°),[37] **1** has a less distorted five-membered ring (dihedral angle: N45–C5–C37–C33 9.4°). However, the structure displays an increased dihedral angle around the C5–C37 bond (dihedral angle: C35–C5–C37–C17 31.2°) due to the formation of a more stable convex form in the solid state.[38]

Stacks of (*P*)- and (*M*)-convex enantiomers are present in the packing arrangement of complex **1**. Unlike some other **Cor**

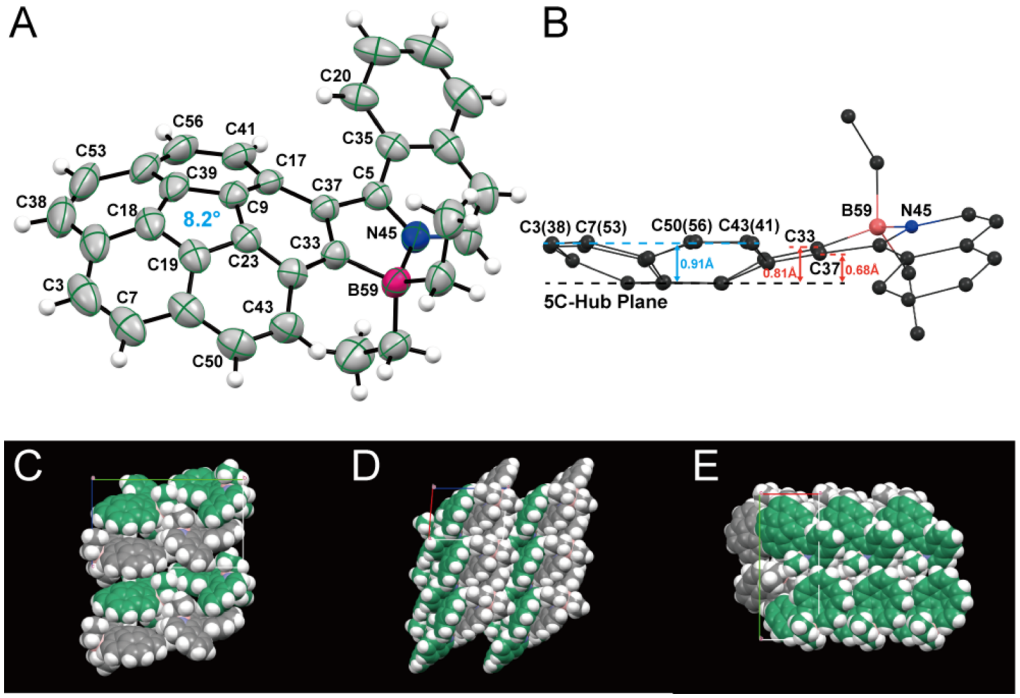

Fig. 1 Molecular structure of **1** [convex (*P*)-enantiomer is shown, top (A)], andORTEP drawings are shown at the 50% probability level. Side view and bowl depth (top (B)). Crystal packing in **1** along the *a* (bottom (C)), *b* (bottom (D)), and *c* (bottom (E)) axes. (*P*)- and (*M*)-enantiomers are colored in green and gray, respectively.

derivatives that pack as columnar stacks in crystal form,[2,3,39] (*P*)- and (*M*)-convex enantiomers of **1** are arranged alternately in a step-like fashion due to the introduced asymmetric helicene part (Fig. 1C–E). Meanwhile, the enantiomers adopt an alternating arrangement to form sheet-like structures with C–H···π interactions (2.911–3.122 Å) between the Ph ring of isoquinoline and corannulene in the concave direction (ESI, Fig. S6B†).

2.3 Electrochemistry and ECL

ECL is a light-emitting process triggered by electrochemical reactions.[40–44] The redox and ECL behaviors of complex **1** were first investigated (Fig. 2) using instrumental set-ups illustrated in Fig. S7A and B.† Fig. 2A displays a typical ECL-voltage curve of 0.6 mM **1** in 1 : 1 benzene : MeCN solution containing 0.1 M tetrabutylammonium hexafluorophosphate ($TBAPF_6$) as the supporting electrolyte, along with its cyclic voltammogram (CV). Complex **1** shows a quasi-reversible reduction at $E^{0'} = -1.67$ V *vs.* SCE to form a radical anion. This observation agrees with the fact that **Cor** can be reduced up to a tetraanion in a series of one-electron reductions, as described by the pioneering work on its reduction reactions with alkaline metals such as Li and K by Rabinovitz and Scott *et al.*[45] The radical anion $\mathbf{1}^{\cdot-}$ is therefore visualized as an aromatic 5C/6e core suspended within an aromatic 15C/15e rim from neutral **1** of the aromatic 5C/6e core within the aromatic 15C/14e rim as in the model "annulene within an annulene". From the DFT calculations shown in the ESI,† it seems that the helix attachment in **1** does contribute to the non-degenerate LUMO. As depicted in Fig. 2A, **1** undergoes oxidation irreversibly at $E_{pa} = 1.21$ V *vs.* SCE to produce a radical

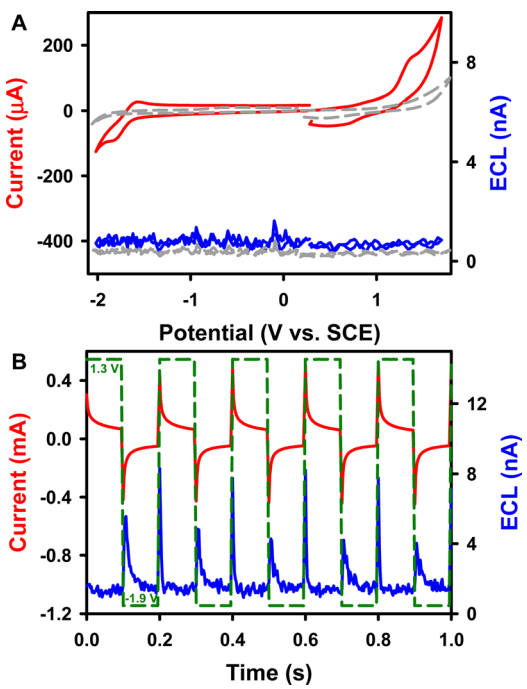

Fig. 2 (A) CV with the ECL-voltage curve of a bare GCE in the absence (dash grey) and presence (solid red and blue) of 0.6 mM **1** in 1 : 1 benzene : MeCN (volume ratio) solution with 0.1 M $TBAPF_6$ as the supporting electrolyte. The CV scan rate was 10 V s^{-1}. (B) The current–time response curve along with the corresponding ECL-time of the electrolyte solutions in (A) during potential pulsing between −1.90 and 1.30 V at a frequency of 10 Hz. The corresponding applied potential profile is illustrated in green.

cation. This irreversibility might be due to Jahn–Teller vibronic distortion caused by corannulene radical cation instability in its original C_{5v} molecular arrangement *via* breaking the degeneracy in HOMOs, similar to the process of removing a π-electron using UV 193 nm photoionization with **Cor** in the gas phase.[46] Again, it seems that the helix attachment in **1** does contribute to the HOMO as observed from the molecular orbital picture in the ESI.†

In the annihilation process where the radical cation and anion meet to react, an emitting excited state is formed if the electrogenerated species of complex **1** have enough energetics and life times. The ECL-voltage curve does not show an appreciable ECL signal in Fig. 2A. In fact, the enthalpy of ECL generation reactions determined from the peak potentials of the redox waves (2.72 eV) is greater than that of the excitons (2.69 eV) determined from the emission peak wavelength:[47,48]

$$E_p(R'/R'^{\bullet+}) - E_p(R/R^{\bullet-}) - 0.16\ (\text{eV}) \geq -\Delta H^\circ \quad (1)$$

where $E_p(R'/R'^{\bullet+})$ and $E_p(R/R^{\bullet-})$ are the oxidation and reduction peak potentials, respectively, obtained from the CV in Fig. 2A; $-\Delta H^\circ$ represents the enthalpy of fluorescence of the excitons. Thermodynamically, it is possible to generate ECL. However, there is no appreciable ECL signal during the potentiodynamic scan in Fig. 2A. Plausibly, due to the irreversibility of anodic oxidation of **1**, the unstable radical cation of **1** cannot survive long enough to meet the radical anion and react, making ECL generation undetectable. This is evidenced by the observation that **1** undergoes an irreversible oxidation reaction even at a fast scan rate at 10 V s^{-1}. Therefore, to shorten the reaction time and allow more radical anions and cations to collide and generate excited states, the potential pulsing ECL experiment with a pulse width of 0.05 s and a pulse cycle at 10 Hz was conducted. Fig. 2B displays the potential pulsing between 1.30 V and −1.90 V, from which greater ECL intensity in both the anodic potential region (∼9 nA) and cathodic one (∼5 nA) can be observed. Again, the radical life time plays a dominant role. Because the rapid fading of the unstable **1** radical cations in the vicinity of the electrode surface reduces its concentration to react with radical anions, weak ECL is generated in the cathodic region. In contrast, complex **1** produces a more chemically stable anion, thus allowing enough time for them to diffuse and interact with the radical cations being generated at the working electrode, and stronger ECL is produced in the positive potential region.

In comparison, the oxidation potential of the parent **Cor** is 1.52 V, and **Cor** undergoes a reversible reduction reaction with a formal potential of −1.62 V and an irreversible reduction at an E_{pc} of −2.51 V (Fig. S8A†); these values agree very well with the values reported by Valenti, Scott, Paolucci and Marcaccio *et al.*[14] The two ethyl groups balance the Lewis acidity of the boron atom, thus increasing the electron density of the **Cor** motif. Additionally, the redox potentials are all negatively shifted. As seen in Fig. S8B,† **Cor** produces no appreciable cathodic ECL but high anodic ECL (∼4.5 nA) during potential pulsing between −2.60 and 1.60 V at a frequency of 10 Hz, which is much stronger than that of the CV scan experiment (∼0 nA).

Table 1 Absolute ECL efficiencies of **Cor** and **1**[a] under various experimental conditions

	Absolute ECL efficiency (%)		
Sample	Coreactant	CV	Pulse
1	Annihilation	—	0.00010 ± 0.00002
	BPO	0.014 ± 0.003	0.025 ± 0.005
Cor	Annihilation	—	0.000017 ± 0.000006
	BPO	0.00060 ± 0.00008	0.0030 ± 0.0006

[a] $Ru(bpy)_3^{2+}$/BPO system: $\Phi_{CV} = 0.53 \pm 0.07\%$; $\Phi_{pulse} = 0.66 \pm 0.04\%$.

This finding also demonstrates that radical anions of **Cor** are more stable than the cations. Moreover, the ECL intensity of **1** is twice as strong as that of **Cor**. The absolute ECL efficiencies of both **Cor** systems during pulsing were determined following the procedure illustrated in the ESI.†[49–51] As presented in Table 1, the absolute ECL efficiency (Φ_{ECL}) of **1** is 0.00010 ± 0.00004%, which is more than 5 times higher than that of **Cor** (0.000017 ± 0.000007%). Possibly, the lower electro-affinity nature of π-extended **1** compared to **Cor** makes it more-readily oxidized to form a stabilized cation for further ECL reactions.

For PAHs such as perylene or pyrene, the principles in ECL studies are the same. For instance, perylenetetracarboxylic diimide (PDI), terrylenetetracarboxylic diimide (TDI), and quaterrylenecarboxylic diimide (QDI) were investigated by Bard *et al.*[52] All these PAH compounds undergo two reversible one-electron reductions and one reversible one-electron oxidation reaction. Their radical stability and reactivity favor the generation of excited states during ECL processes.

The effect of inversion motions of both the bowl and the helix on ECL luminescence will be discussed later in more detail.

2.4 ECL with benzoyl peroxide (BPO) as the coreactant

To further improve ECL performances, benzoyl peroxide (BPO) has been used as a coreactant with complex **1** (Fig. 3) in the reductive-oxidation mode[14,53–55] due to high stability of the **1** radical anion as described above. Fig. 3A illustrates the ECL-voltage curve of 0.6 mM **1** with the corresponding CV in the presence of 5 mM BPO in 1 : 1 benzene : MeCN solution. The onset of the ECL potential of the complex **1**/BPO system is at about −1.62 V, right at the reduction of **1**, and the ECL intensity reaches up to a maximum of 134 nA. Similarly, the onset ECL of the **Cor**/BPO system is located at −1.68 V, approaching a maximum ECL intensity of 5 nA, which is much lower than that of the **1**/BPO system (Fig. S9A†). The absolute ECL efficiencies of these two corannulene complex-BPO systems during a CV scan were determined as illustrated in the ESI.† As displayed in Table 1, the Φ_{ECL} of the **1**/BPO system is 0.014 ± 0.003%, which is more than 23 times higher than that of the **Cor**/BPO system (0.00060 ± 0.00008%).

Fig. 3B and S9B† show current–time and the corresponding ECL-time curves of 0.6 mM **1** and **Cor** in the presence of 5 mM BPO during a potential pulsing experiment at a frequency of 10 Hz. Notably, the pulsed-ECL of complex **1** with BPO (1.8 μA)

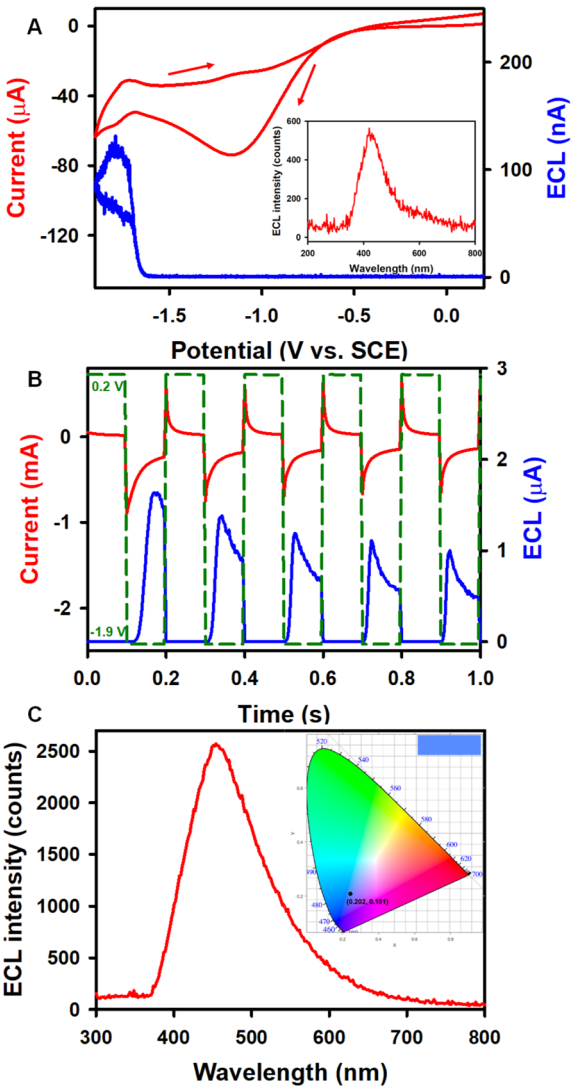

Fig. 3 (A) CV with the ECL-voltage curve of 0.6 mM **1** in the presence of 5 mM BPO in 1 : 1 benzene : MeCN (volume ratio) solution with 0.1 M $TBAPF_6$ as the supporting electrolyte. The CV scan rate was 100 mV s^{-1}. (B) The current–time response along with the corresponding ECL-time curve of 0.6 mM **1** in the presence of 5 mM BPO during a potential pulsing experiment between 0.2 and −1.90 V at a frequency of 10 Hz. (C) The accumulated ECL spectrum of the potential pulsing experiment. The insets show the CIE coordinate diagram of the ECL spectrum.

is much stronger than that of the **Cor**/BPO coreactant system (0.8 μA), while the absolute ECL efficiency of the **1**/BPO system (0.025 ± 0.005%) is more than 8 times higher than that of the **Cor**/BPO system (0.003 ± 0.0006%) (Table 1). Furthermore, the pulsed-ECL of these two corannulene complex/BPO systems demonstrates higher absolute ECL efficiencies compared with their CV-ECL in the coreactant route. Valenti, Scott, Paolucci and Marcaccio *et al.*[14] obtained an intense ECL signal qualitatively with the 1 mM **Cor**/10 mM BPO coreactant system in acetonitrile solution. Please note that we report absolute ECL quantum efficiencies here, which are more quantitative. For comparison, the absolute quantum efficiency for the ECL gold standard, $Ru(bpy)_3^{2+}$, was determined to be $\Phi_{ECL\text{-}CV}$ = 0.53 ± 0.07% and $\Phi_{ECL\text{-}pulse}$ = 0.66 ± 0.04% with BPO as the coreactant, which has been taken as 5% conventionally. Anyway, although the absolute ECL quantum efficiencies of the **1**/BPO system are lower than those of the $Ru(bpy)_3^{2+}$/BPO system, **1** represents a much stronger luminophore than **Cor** for ECL. This work still provides insight into development of new **Cor** compounds for ECL applications.

In addition, **Cor** generates ECL immediately when the potential is switched on in the first cycle, while there is an obvious delay (up to 0.02 s) for **1** to produce ECL. The reason might be that after the reduction of **1**, repulsion would occur between the radical anions of **1** carrying negative charges and the working cathode electrode, which could accelerate the radicals to the diffusion layer to react with benzoyl radicals and emit ECL. Ultimately, shorter time intervals result in fewer decayed radicals and higher ECL efficiency.

2.5 Spooling ECL spectroscopy

Fig. 4 and S9D† present the spooling ECL spectra of complexes **1** and **Cor** acquired during a CV scan upon addition of 5 mM BPO as the coreactant in the above systems. Of note, spooling ECL spectroscopy was performed by recording ECL spectra at certain time intervals during ECL generation processes,[56] as previously reported by our group elsewhere. The spooling ECL spectra of both coreactant systems illustrate the evolution and devolution of the ECL process on the basis of the two proposed mechanisms. Taking complex **1** as an example, in both mechanisms, ECL is produced at −1.62 V where the **1** radical anion is generated, which aligns with the ECL-voltage curves in Fig. 3A. In Fig. 4 and S9D,† the spectra of complex **1** and **Cor** display consistent peak shapes and peak wavelengths during potential scans, revealing that the excited states are independent of applied potentials, thus providing evidence that an identical excited state generates ECL during the annihilation and coreactant processes. Fig. 5 illustrates the mechanisms of the coreactant ECL route with BPO. Strongly oxidizing benzoate radicals ($PhCOO^{\bullet}$) appear after the reduction of BPO. In one way, these radicals can oxidize the radical anions of **1** produced at −1.62 V to generate the **1*** excited state that emits ECL right at −1.62 V (Fig. 5A). Conversely, $PhCOO^{\bullet}$ can also oxidize the neutral **1**, and then generate radical cations of **1**, which thereafter react with the radical anions of **1** to generate the excited state emitting ECL at −1.62 V (Fig. 5B). Thereby, spooling ECL spectroscopy is a powerful tool to reveal the kinetics and mechanisms of ECL processes.[49]

2.6 Absorption and luminescence spectroscopy

During the CV and the potential pulsing experiments, accumulated ECL spectra of **1** were acquired. As shown in Fig. 3A (inset) and 3C, the ECL peak wavelengths of **1** in both annihilation and coreactant pathways are 454 nm, while the ECL peak wavelength of **Cor** is located at 412 nm (Fig. S9C†). The UV-vis absorption and PL studies of 0.02 mM **Cor** and **1** were also carried out in 1 : 1 benzene : MeCN solution. As seen in Fig. 6A, the UV-vis absorption spectrum of **1** shows maxima at 424, 402, 386, and 309 nm, with a shoulder-like absorption at around

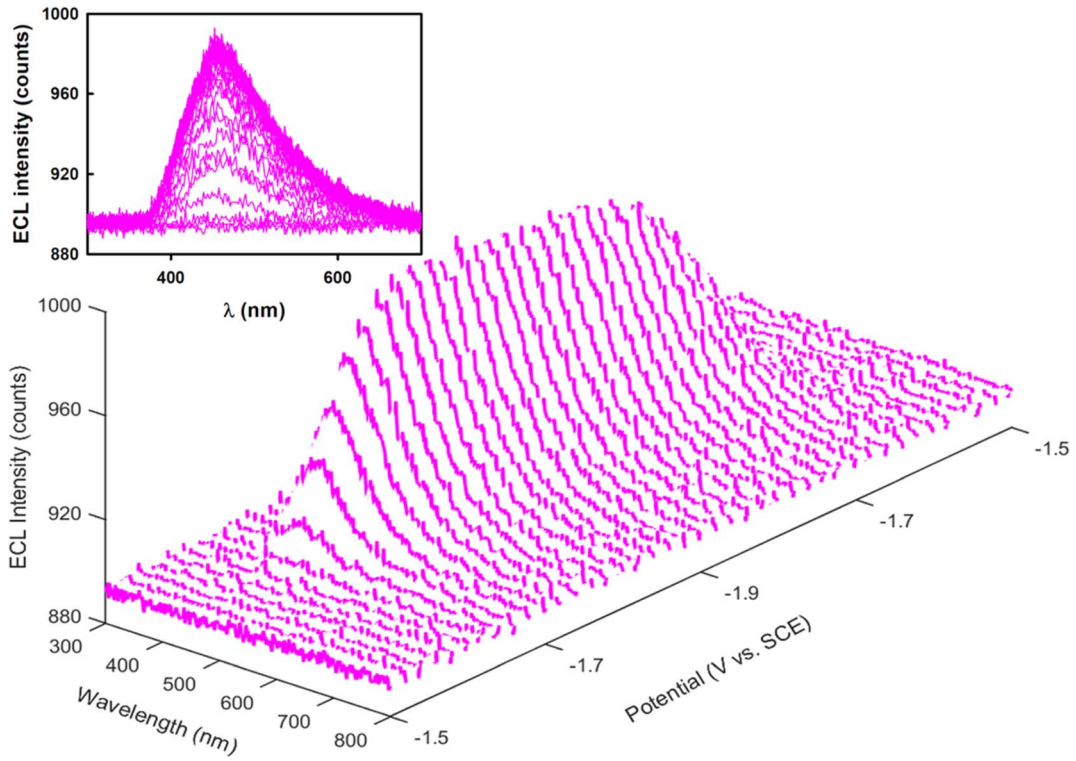

Fig. 4 Spooling ECL spectra of 0.6 mM **1** in the presence of 5 mM BPO in potential ranges between 0.2 and −1.9 V. Inset shows the 2D viewing of the spooling ECL spectra.

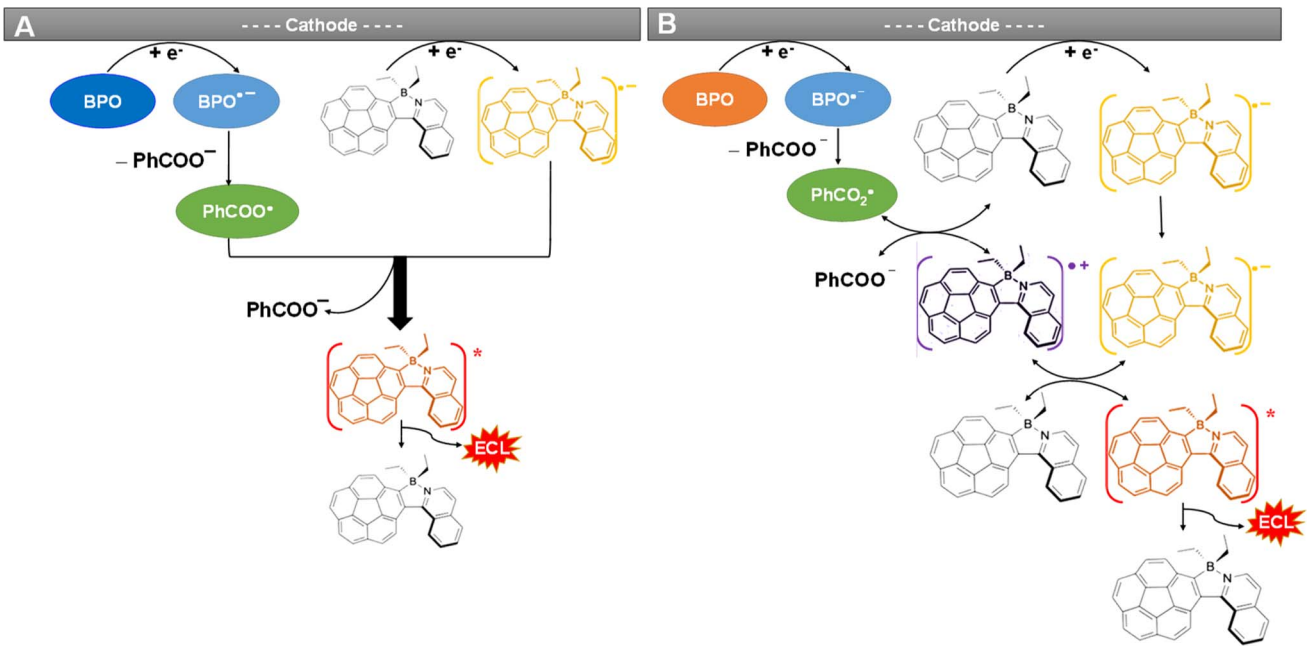

Fig. 5 Two mechanisms (A, B) of the coreactant ECL route with BPO.

340 nm. The PL maxima appear at 461 and 447 nm, and the absolute PL quantum yield (Φ_{PL}) for the complex **1** is 31% (detailed determination process is given in ESI†). The Commission International de l'Éclairage (CIE) coordinates of **1** were calculated to be (0.202, 0.181) and (0.140, 0.112) based on the ECL and PL spectra, respectively. Moreover, the ECL and PL with **1** both show blue emission, as displayed in the top right corner of the CIE diagrams. The UV-vis absorption and PL spectra of **Cor** were also recorded. As seen in Fig. S10A,† **Cor** exhibits a major absorption band at around 289 nm and a PL

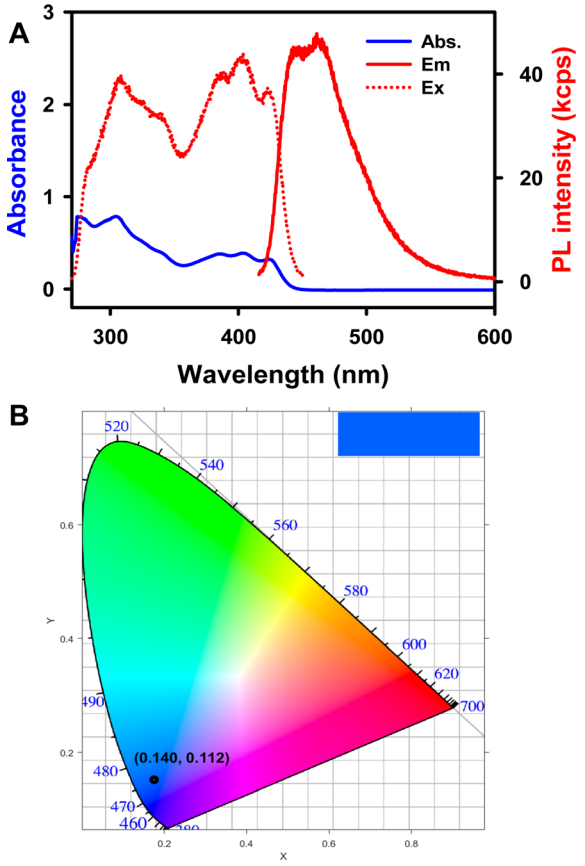

Fig. 6 (A) UV-visible absorption and photoluminescence spectra of 5 μM **1** in 1 : 1 benzene : MeCN (volume ratio) solution, $\lambda_{ex} = 403$ nm and $\lambda_{em} = 451$ nm. (B) The CIE coordinate diagram of the PL spectrum.

emission with a peak wavelength of 423 nm ($\Phi_{PL} = 1.0\%$), which is similar to the ECL variation ratio. The observation of blue luminescence in the CIE diagram (Fig. S10B†) is consistent with the literature reports.[14] The ECL spectra are in good agreement with the PL, revealing that both PL and ECL rise from the same excited state. It is interesting to note that the HOMO–LUMO gaps from the DFT calculations (ESI†) is 3.51 and 4.40 eV for **1** and **Cor**, respectively. Compound **1** breaks the C_{5v} symmetry for **Cor**, and the HOMO and LUMO lose the degeneracy, leading to a decreased HOMO–LUMO energy gap. Symmetry-breaking causes a decrease in the HOMO–LUMO energy gap, increase in the emission peak wavelength and increase in the PL quantum yield. These tendencies are very similar to those of 5,10,15,20-tetraphenyl-21*H*,23*H*-porphine zinc (ZnTPP) and 5,10,15,20-tetraphenyl-21*H*,23*H*-porphine (H_2TPP).[57]

2.7 Chemiluminescence

The CL properties of complexes **1** and **Cor** were explored through excitation by assessing the chemical energy released during the reaction of a phenyl peroxyoxalate ester with hydrogen peroxide (instrumentation is shown in Fig. S7C†). In Fig. 7A, bright blue CL emission can be visually observed in a dark room after adding 0.25 mL 30% H_2O_2 to 1 mL of a 4 : 1 *N*,*N*-dimethylformamide (DMF) : MeCN (volume ratio) solution containing 1.5 mg per mL **1**, 10 mg per mL bis(2,4,5-trichloro-6-(pentyloxycarbonyl)phenyl)-oxalate (CPPO) and 2 mg per mL sodium salicylate. As illustrated in Fig. S11,† CPPO reacts with H_2O_2 in the presence of a base catalyst (sodium salicylate) to generate oxalyl chloride and produce a high-energy intermediate (1,2-dioxetanedione), which finally decomposes into CO_2.[58] The released energy from this exothermic reaction can support the production of **1*** from complex **1**. Subsequently, the relaxation of **1*** to its ground state generates CL emission. The difference between CL and ECL is that the energy in the CL reaction required to generate emissive excited state species originates from chemical reactions instead of an electrical current, which is more convenient and faster than ECL.[51,59–61]

Spooling CL spectroscopy was utilized to monitor CL evolution and devolution processes, which we have demonstrated for a thermally activated delayed fluorescence emitter, porphyrin, as well as luminol, graphene quantum dots and other luminophores.[55,58,61,62] Fig. 7D displays the spooling CL spectra of this reaction system, where each spectrum was collected for 1 s for a total time of 30 s. With the addition of H_2O_2 into a solution containing **1**, CPPO and sodium salicylate, the broad emission peaks are centered at 472 nm and they are independent of the time (Fig. 7B). The calculated color with coordinates of (0.167, 0.329) (Fig. 7C) from the CIE color diagram matches well with the photograph (Fig. 7A). All above results closely match the emission observed in the PL and ECL in the coreactant pathway, suggesting that a single excited state of **1** is produced in these three excitation strategies. Thus, complex **1** is a promising luminophore in various light-emitting applications.

Notably, a relatively weak blue CL emission (Fig. S12A†) can be observed by the naked eyes in a dark room after adding 1 mL 30% H_2O_2 to 1 mL of a 4 : 1 DMF : MeCN solution containing 6 mg per mL **Cor**, 40 mg per mL CPPO and 2 mg per mL sodium salicylate, with the concentration being 4 times higher than that of **1**. Moreover, the CL intensity of **Cor** is so weak that it could not be detected by the same spectrometer even using a higher concentration solution. In turn, the CL light of **Cor** was measured by using a spectrograph/CCD camera setup, as illustrated in Fig. S7D.† A weak emission peak can be observed at 434 nm, and the CL intensity of **Cor** shown in Fig. S12B† is much smaller than that of complex **1**. As shown in the CIE color diagrams, the CL emission has coordinates of (0.244, 0.241) (Fig. S12C†), correlating with the photograph. These results also closely match the emission observed in the PL and ECL coreactant pathways, leading to the conclusion that one excited state is observed here.

The absolute CL quantum efficiency (Φ_{CL}) is defined as the number of photons produced per CPPO molecule, which is the limiting species in this CL reaction.[51,58,61] The number of photons per spectrum can be determined by using a spectrometer (USB2000+, Ocean Insight, Orlando, FL) after integration of each spectrum in the wavelength range of interest (400–700 nm), as descripted in the ESI.† The total number of photons can be determined by summing each spooling CL spectrum over the entire experiment. The Φ_{CL} of complex **1** was determined as displayed in Table 2. The Φ_{CL} increased gradually on increasing the solution concentrations and reached a maximum value of

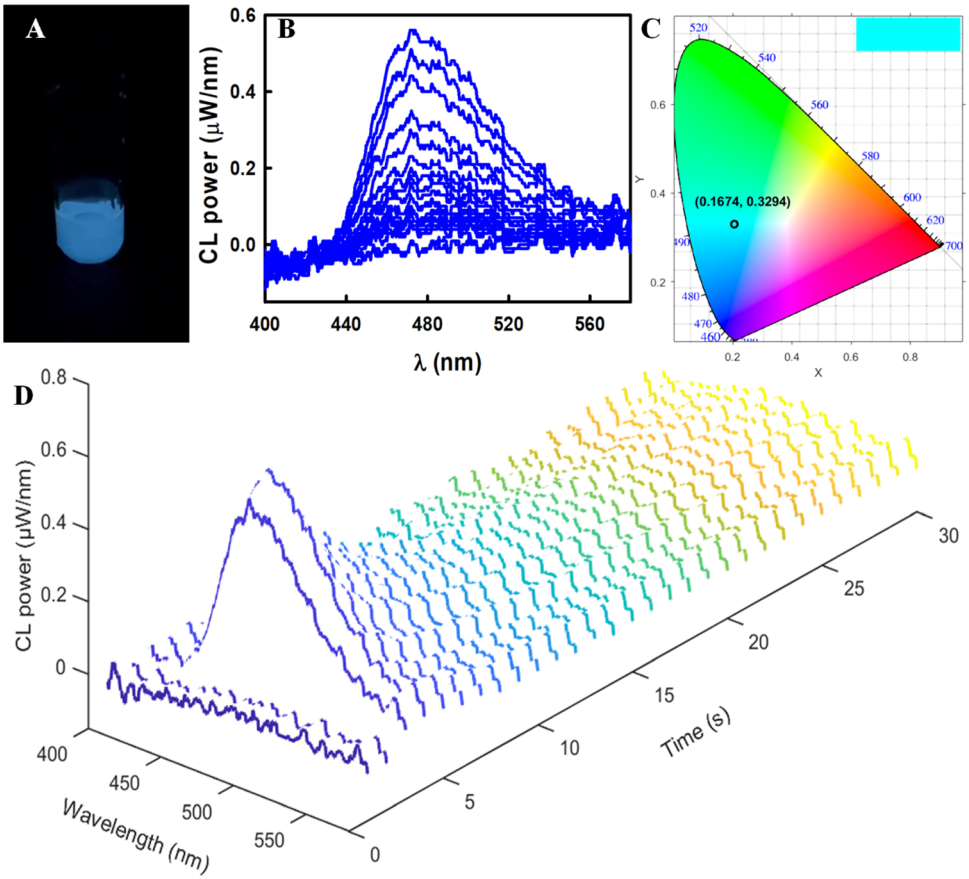

Fig. 7 (A) Photos, (B) 2D view of stacked spooling CL spectra demonstrating consistent shapes and peak wavelengths, (C) CIE coordinate diagram of the CL spectrum, and (D) spooling CL spectra acquired at a time interval of 1 s in the presence of **1**, CPPO and H_2O_2. Conditions: adding 0.25 mL 30% H_2O_2 in acetonitrile to 1 mL of an 80% DMF, 20% acetonitrile solution containing 1.5 mg per mL **1**, 10 mg per mL CPPO and 2 mg per mL sodium salicylate.

Table 2 Absolute CL efficiency of **Cor** and **1**[a]

Sample	Concentration (mg)	CPPO (mg)	Total photons	Absolute CL efficiency (%)
1	1.0	6.7	2.24×10^{14}	0.0040 ± 0.0005
	1.5	10	6.76×10^{14}	0.0080 ± 0.0008
	3.0	20	3.52×10^{15}	0.020 ± 0.004
	6.0	40	7.10×10^{15}	0.020 ± 0.002
Cor	6.0	40	2.88×10^{14}	0.00080 ± 0.00007

[a] $Ru(bpy)_3^{2+}$: $\Phi_{CL} = 0.00009 \pm 0.00001\%$.[51]

0.020% ± 0.004, which is 222 times greater than that of $Ru(bpy)_3^{2+}$ (Φ_{CL} = 0.00009 ± 0.00001%).[51] To obtain a μW-wavelength curve, the CL spectrum measured on the CCD camera was then divided by the conversion curve as we reported earlier (Fig. S12D, further details are in the ESI†).[7] However, the Φ_{CL} of **Cor** is only 0.00080 ± 0.00007%, which is 25 times lower than that of **1**. In comparison with classical PL, the concentrations of various substances should be considered in the study of optical properties of CL and ECL, because their reactions usually involve several reactants. Detection limits for CL and ECL should be much lower than that of PL, since no light source is needed for CL and ECL.

2.8 Dynamic inversion behaviors

Azaborahelicene corannulene **1** undergoes two types of inversion motions: bowl and helix inversions, leading to four stereoisomers. The details are illustrated in Fig. 8. NMR chemical shifts of all the three protons (H_a and H_b in CH_2 and others in CH_3) in ethyl groups on **1** at room temperature were assigned to multiple peaks between 1.00 and 0.90 ppm, a single peak at 1.17 ppm and a single peak at 0.19 ppm, respectively, as shown in the spectrum at 298 K in Fig. 9. These three types of protons are situated in different chemical environments, with spatial proximity to the corannulene and helix motifs. It is

anticipated that slowing down the inversion at a lower temperature will lead to splits of the three proton chemical shifts. To understand the effects of bowl and helix dynamic inversions in molecule **1** on its CL and ECL efficiencies, variable-temperature (VT) ^{1}H NMR experiments were performed in CD_2Cl_2 at 600 MHz, covering a temperature range from 298 K to 188 K with 10 K increments (Fig. 9). Select spectra also were acquired upon heating back from 188 K to 298 K, which showed that all the dynamic processes were reversible (Fig. S13†). Depending on the rate of bowl and helix inversion processes in **1** on the NMR timescale, the protons of two ethyl groups situated in different chemical environments could split to two sets of signals. VT ^{1}H NMR spectra acquired at a decreased temperature are a bit complicated; the H_b and CH_3 signals in closer spatial proximity to the helix motif exhibited nearly identical coalescence temperatures (~273 K), while the H_a signal situated near the corannulene motif showed a significantly lower coalescence temperature (238 K). A plausible explanation is that the stereoisomerism caused by helicene inversion (*P*/*M* isomers) predominantly influences the chemical environments of H_b and CH_3 hydrogens, while the effects of stereoisomerism due to bowl inversion (convex/concave isomers) are negligible. The situation is precisely the reverse for H_a. A simple conclusion was quite clear: H_b and CH_3 signals in VT ^{1}H NMR spectra were mainly affected by the helicene inversion process, while H_a signals were mainly influenced by the bowl inversion process, as illustrated by Fig. S17.† A detailed explanation can be found in the section "More details on ^{1}H NMR analysis" in the ESI.† This surprising discovery enabled the observation of the bowl and helix inversion processes of complex **1** in the VT ^{1}H NMR spectra simultaneously, as shown in Fig. 9. In the literature, Scott *et al.*[5] utilized dimethylcarbinol and Siegel *et al.*[7] used ethyl to probe corannulene bowl-to-bowl inversion. For the first time, we employed H_b, CH_3, and H_a to probe the inversions of both the helicene and bowl, respectively.

Dynamic ^{1}H NMR line-shape simulations were conducted to determine the values of the rate constants (k) at various temperatures and to estimate the coalescence temperature (T_c) value of both bowl and helix inversion of **1**.[7,63] The Eyring equation ($\Delta G_c^{\ddagger} = -RT\ln(kh/k_BT)$) was then used to calculate $\Delta G_c^{\ddagger}$ values at coalescence temperature T_c, and the Eyring plot was used to determine $\Delta H^{\ddagger}$ and $\Delta S^{\ddagger}$ values. The equation, $\Delta G^{\ddagger} = \Delta H^{\ddagger} - T\Delta S^{\ddagger}$, was used to calculate the $\Delta G_{298K}^{\ddagger}$ values at room temperature (298 K) for comparing energy barriers. (see ESI Fig. S13–S16† for more details).

The energy barriers $\Delta G_{298K}^{\ddagger}$ of helix motif inversion in **1** are experimentally found to be 12.0 kcal mol^{-1} for CH_3 signals and 12.9 kcal mol^{-1} for H_b signals. A value of 12.0 kcal mol^{-1} is chosen for the energy barrier of helix motif inversion, as helix inversion is more responsive to changes in the chemical environment and aligns more accurately with the Eyring plot, as shown in Fig. S14, S16A andB.† Besides, the energy barrier $\Delta G_{298K}^{\ddagger}$ of the bowl inversion is experimentally found to be 12.7 kcal mol^{-1}, reflecting the steric influence of the helix motif on the corannulene motif during the inversion process. The first experimental bowl inversion energy barrier of corannulene with diastereotopic protons was determined to be 10.2 kcal mol^{-1} by Scott *et al.* in 1992, which corresponds to 200 000 times inversion per second at room temperature.[5] **Cor** should have faster bowl inversions. In comparison, the determined rates of helix

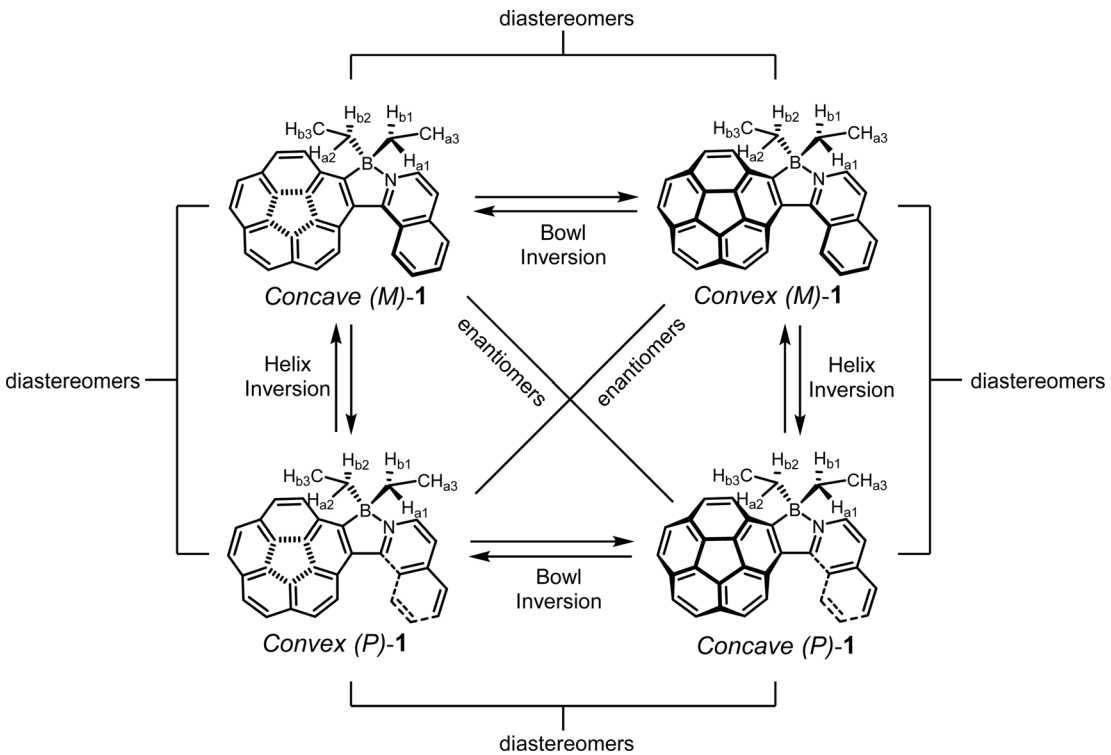

Fig. 8 Inversion pathways of compound **1**.

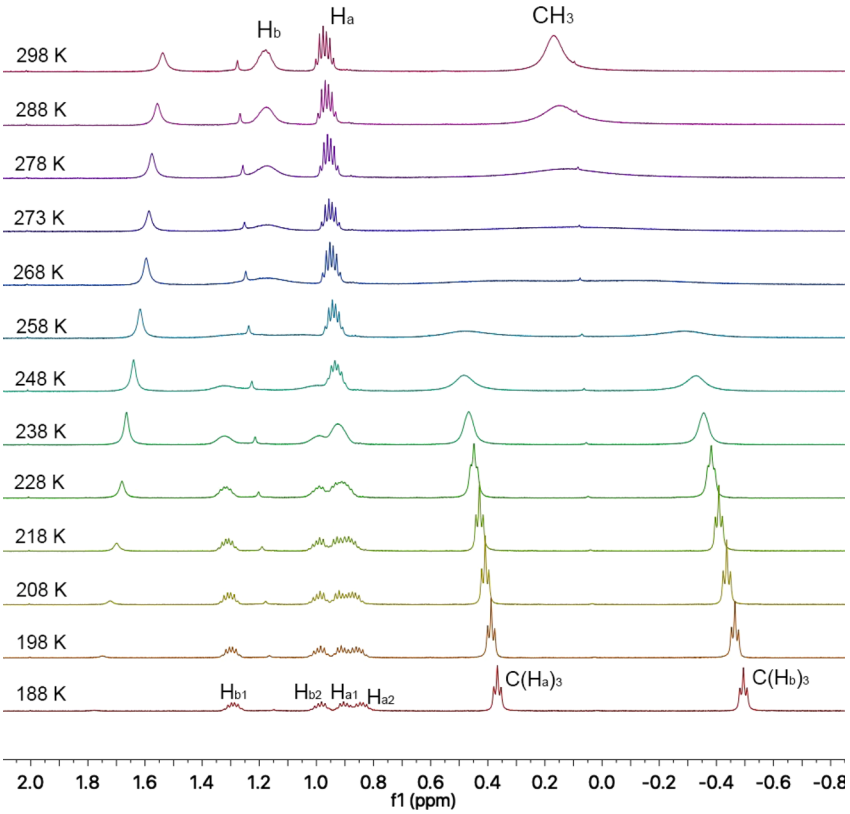

Fig. 9 NMR spectroscopy of molecule **1**. Stacked spectra for variable-temperature ^{1}H NMR (600 MHz) spectroscopic measurements of **1** in CD_2Cl_2. T_c values (coalescence temperature) of ^{1}H resonances for H_a protons were determined to be 238 K for bowl inversion and those of H_b and CH_3 protons were determined to be 268 K and 273 K for helix inversion.

and bowl inversion in **1** at room temperature are 10 000 and 3000 times per second, respectively. This observation indicates that the introduction of the azaborahelical structure effectively decelerates the inversion rate of the corannulene motif. As the dynamic inversion behavior of corannulene was found to increase non-radiative loss of excited energy, the enhanced CL, ECL, and PL efficiencies of **1**, as compared to those of **Cor**, are partially attributed to the restricted bowl-to-bowl inversion motions. Restriction of intramolecular inversion motions (RIIM) in complex **1** is similar to the aggregation-induced emission (AIE) and crystallization-induced ECL (CIECL),[19,23,64] where restricted intramolecular rotations (RIR) lead to reduction in excited state energy loss. However, the luminescence efficiencies in this case are enhanced through a distinct mechanism. This study is the first to experimentally demonstrate that luminescence efficiency can be increased by RIIM, offering not just a complementary route to existing emission enhancement strategies but also paving the way for innovative designs in luminescent materials based on bowl-shaped aromatic hydrocarbons with enhanced efficiencies and functionalities.

3 Conclusions

In summary, we have designed and synthesized an azabora[5]helicene corannulene **1** by introducing isoquinoline as a chelating ligand and further bridged by using boron with an electrophilic aromatic borylation. The azabora-helicene–corannulene hybrid structure was further confirmed by X-ray crystallography. As expected, the rationally designed **1** produced a strong blue light emission. Specifically, **Cor** hybrid **1** showed a notable increase in absolute PL quantum yield, increasing from 1% to 31%, and absolute quantum efficiencies of CL, and ECL using benzoyl peroxide as a coreactant, increasing from 0.0008% to 0.02%, and 0.003% to 0.025%, respectively. Furthermore, the mutually influencing inversion motions of the bowl and helix motifs in **1** were investigated through VT ^{1}H NMR technology, revealing that the bowl inversion rate was effectively decelerated by a steric repulsion effect of the helix motif, which contributed to enhanced CL, ECL and PL efficiencies *via* reducing the non-radiative loss of excited state energy. This enhancement in luminescence caused by reduction in bowl inversion is an alternative way to mimic AIE and crystallization-induced ECL (CIECL) phenomena caused by restricted intramolecular rotations. Although the all-carbon corannulene–helicene hybrid reported by Scott *et al.*[65] is more rigid than **1**, it doesn't mean the bowl-to-bowl inversion could be better lowered as the π-extended rigid helix motif could further flatten the bowl structure and facilitate the inversion process of the corannulene motif. These findings provide fundamental insights into enhancing quantum efficiencies by rationally modulating the molecular structure and geometry of

corannulene-based species. Meanwhile, utilizing these enhanced corannulene derivatives with a suitable coreactant opens a new path for the future development of efficient light-emitting devices and diagnostic immunoassays.

Data availability

Original experimental data is available upon request.

Author contributions

Z. D. and J. H. conceived and directed the project and designed the experiments. X. Q., L. H. and Z. Z. performed all the experiments and analyzed the results. L. H. carried out the crystallographic studies and Q. W. performed the DFT calculations. X. Q., L. H. and Z. D. prepared the manuscript. Z. D. finalized the paper.

Conflicts of interest

There are no conflicts to declare.

Acknowledgements

This research was supported by the Natural Sciences and Engineering Research Council of Canada [NSERC, DG RGPIN-2013-201697, DG RGPIN-2018-06556, DG RGPIN-2023-05337 and SPG STPGP-2016-493924 (Z. D.)], New Frontiers in Research Fund [NFRFR-2021-00272 (Z. D.)], National Natural Science Foundation of China [22004034 (X. Q.)], and the China Scholarship Council [CSC, 201908430010 (X. Q.)]. L. H., P. F., and J. H. gratefully acknowledge the National Natural Science Foundation of China (NSFC) (grant number 21672159) and the National Program on Key Basic Research Project of China (973 Program) (2015CB856500). We appreciate the leadership and knowledge on synthesis and quantum chemistry of corannulenes provided by Drs Jay Siegel and Kim Baldridge during their time at Tianjin University. We also acknowledge the Electronic Shop, the NMR facility manager Dr Mathew Willans in the Department of Chemistry, and Science Stores at Western University for their great service. Prof. Ruizhong Zhang at Tianjin University is acknowledged for providing various help. Dedicated to Prof. Allen J. Bard for his more than 5 decades' pioneering contributions to electrochemical science.

References

1 T. Guo, A. Li, J. Xu, K. K. Baldridge and J. Siegel, *Angew. Chem., Int. Ed.*, 2021, **60**, 25809–25814.
2 X. Tian, J. Xu, K. K. Baldridge and J. S. Siegel, *Angew. Chem., Int. Ed.*, 2020, **59**, 1460–1464.
3 Y. T. Wu, D. Bandera, R. Maag, A. Linden, K. K. Baldridge and J. S. Siegel, *J. Am. Chem. Soc.*, 2008, **130**, 10729–10739.
4 A. Borchardt, A. Fuchicello, K. V. Kilway, K. K. Baldridge and J. S. Siegel, *J. Am. Chem. Soc.*, 1992, **114**, 1921–1923.
5 L. T. Scott, M. M. Hashemi and M. S. Bratcher, *J. Am. Chem. Soc.*, 1992, **114**, 1920–1921.
6 T. J. Seiders, K. K. Baldridge, E. L. Elliott, G. H. Grube and J. S. Siegel, *J. Am. Chem. Soc.*, 1999, **121**, 7439–7440.
7 M. Juricek, N. L. Strutt, J. C. Barnes, A. M. Butterfield, E. J. Dale, K. K. Baldridge, J. F. Stoddart and J. S. Siegel, *Nat. Chem.*, 2014, **6**, 222–228.
8 T. J. Seiders, K. K. Baldridge, G. H. Grube and J. S. Siegel, *J. Am. Chem. Soc.*, 2001, **123**, 517–525.
9 A. Ayalon, M. Rabinovitz, P.-C. Cheng and L. T. Scott, *Angew. Chem., Int. Ed.*, 1992, **31**, 1636–1637.
10 A. V. Zabula, A. S. Filatov, S. N. Spisak, A. Y. Rogachev and M. A. Petrukhina, *Science*, 2011, **333**, 1008–1011.
11 A. Ayalon, A. Sygula, P. C. Cheng, M. Rabinovitz, P. W. Rabideau and L. T. Scott, *Science*, 1994, **265**, 1065–1067.
12 C. Bruno, R. Benassi, A. Passalacqua, F. Paolucci, C. Fontanesi, M. Marcaccio, E. A. Jackson and L. T. Scott, *J. Phys. Chem. B*, 2009, **113**, 1954–1962.
13 J. Mack, P. Vogel, D. Jones, N. Kaval and A. Sutton, *Org. Biomol. Chem.*, 2007, **5**, 2448–2452.
14 G. Valenti, C. Bruno, S. Rapino, A. Fiorani, E. A. Jackson, L. T. Scott, F. Paolucci and M. Marcaccio, *J. Phys. Chem. C*, 2010, **114**, 19467–19472.
15 J. S. Ham, *J. Chem. Phys.*, 1953, **21**, 756–758.
16 J. Dey, A. Y. Will, R. A. Agbaria, P. W. Rabideau, A. H. Abdourazak, R. Sygula and I. M. Warner, *J. Fluoresc.*, 1997, **7**, 231–236.
17 C. Si, T. Wang, A. K. Gupta, D. B. Cordes, A. M. Z. Slawin, J. S. Siegel and E. Zysman-Colman, *Angew. Chem., Int. Ed.*, 2023, **62**, e202309718.
18 J. D. Luo, Z. L. Xie, J. W. Y. Lam, L. Cheng, H. Y. Chen, C. F. Qiu, H. S. Kwok, X. W. Zhan, Y. Q. Liu, D. B. Zhu and B. Z. Tang, *Chem. Commun.*, 2001, 1740–1741, DOI: 10.1039/B105159h.
19 B. Z. Tang, Z. Zhao, H. Zhang and J. W. Y. Lam, *Angew. Chem., Int. Ed.*, 2020, **59**, 9888–9907.
20 M. Grandl, Y. Sun and F. Pammer, *Org. Chem. Front.*, 2018, **5**, 336–352.
21 Y. Min, C. Dou, D. Liu, H. Dong and J. Liu, *J. Am. Chem. Soc.*, 2019, **141**, 17015–17021.
22 R. Zhao, C. Dou, Z. Xie, J. Liu and L. Wang, *Angew. Chem., Int. Ed.*, 2016, **55**, 5313–5317.
23 Z. Huang, S. Wang, R. D. Dewhurst, N. V. Ignat'ev, M. Finze and H. Braunschweig, *Angew. Chem., Int. Ed.*, 2020, **59**, 8800–8816.
24 S. K. Mellerup and S. Wang, *Trends Chem.*, 2019, **1**, 77–89.
25 D. Frath, J. Massue, G. Ulrich and R. Ziessel, *Angew. Chem., Int. Ed.*, 2014, **53**, 2290–2310.
26 A. Wakamiya, T. Taniguchi and S. Yamaguchi, *Angew. Chem., Int. Ed.*, 2006, **45**, 3170–3173.
27 L. Jiang, Y. Wang, D. Tan, X. Chen, T. Ma, B. Zhang and D.-T. Yang, *Chem. Sci.*, 2022, **13**, 5597–5605.
28 Z. Dominguez, R. Lopez-Rodriguez, E. Alvarez, S. Abbate, G. Longhi, U. Pischel and A. Ros, *Chem.–Eur. J.*, 2018, **24**, 12660–12668.
29 S. J. Cyvin, E. Brendsdal, J. Brunvoll and M. Skaret, *J. Mol. Struct.*, 1991, **247**, 119–127.

30 Y. Wang, H. Jiang, X. Liu, J. Xu, Y. Gao and N. S. Finney, *Chem. Commun.*, 2021, **57**, 5818–5821.
31 N. Ishida, T. Moriya, T. Goya and M. Murakami, *J. Org. Chem.*, 2010, **75**, 8709–8712.
32 J. C. Hanson and C. E. Nordman, *Acta Crystallogr., Sect. B: Struct. Crystallogr. Cryst. Chem.*, 1976, **32**, 1147–1153.
33 T. J. Seiders, K. K. Baldridge, G. H. Grube and J. S. Siegel, *J. Am. Chem. Soc.*, 2001, **123**, 517–525.
34 R. C. Haddon, *Science*, 1993, **261**, 1545–1550.
35 R. C. Haddon, *J. Phys. Chem. A*, 2001, **105**, 4164–4165.
36 H. Becker, L. T. Scott and D. K. Bohme, *Int. J. Mass Spectrom. Ion Processes*, 1997, **167–168**, 519–524.
37 V. F. Pais, M. M. Alcaide, R. Lopez-Rodriguez, D. Collado, F. Najera, E. Perez-Inestrosa, E. Alvarez, J. M. Lassaletta, R. Fernandez, A. Ros and U. Pischel, *Chem.–Eur. J.*, 2015, **21**, 15369–15376.
38 T. Fujikawa, D. V. Preda, Y. Segawa, K. Itami and L. T. Scott, *Org. Lett.*, 2016, **18**, 3992–3995.
39 Z.-Y. Guo, C.-X. Li, M. Gao, X. Han, Y.-J. Zhang, W.-J. Zhang and W.-W. Li, *Angew. Chem., Int. Ed.*, 2021, **60**, 2.
40 J. Descamps, C. Colin, G. Tessier, S. Arbault and N. Sojic, *Angew. Chem., Int. Ed.*, 2023, **62**, e202218574.
41 Y. Wang, J. Ding, P. Zhou, J. Liu, Z. Qiao, K. Yu, J. Jiang and B. Su, *Angew. Chem., Int. Ed.*, 2023, **62**, e202216525.
42 K. Wu, R. Chen, Z. Zhou, X. Chen, Y. Lv, J. Ma, Y. Shen, S. Liu and Y. Zhang, *Angew. Chem., Int. Ed.*, 2023, **62**, e202217078.
43 X. Wei, M. J. Zhu, Z. Cheng, M. Lee, H. Yan, C. S. Lu and J. J. Xu, *Angew. Chem., Int. Ed.*, 2019, **58**, 3162–3166.
44 W. Guo, H. Ding, C. Gu, Y. Liu, X. Jiang, B. Su and Y. Shao, *J. Am. Chem. Soc.*, 2018, **140**, 15904–15915.
45 M. Baumgarten, L. Gherghel, M. Wagner, A. Weitz, M. Rabinovitz, P.-C. Cheng and L. T. Scott, *J. Am. Chem. Soc.*, 1995, **117**, 6254–6257.
46 H. A. Galué, C. A. Rice, J. D. Steill and J. Oomens, *J. Chem. Phys.*, 2011, **134**, 054310.
47 N. E. Tokel, C. P. Keszthelyi and A. J. Bard, *J. Am. Chem. Soc.*, 1972, **94**, 4872–4877.
48 L. Yang, L. Dong, D. Hall, M. Hesari, Y. Olivier, E. Zysman-Colman and Z. Ding, *SmartMat*, 2022, **4**, e1149.
49 J. R. Adsetts, K. Chu, M. Hesari, J. Ma and Z. Ding, *Anal. Chem.*, 2021, **93**, 11626–11633.
50 A. Fracassa, C. Mariani, M. Marcaccio, G. Xu, N. Sojic, G. Valenti and F. Paolucci, *Curr. Opin. Electrochem.*, 2023, **41**, 101375.
51 Z. Zhan, X. Qin, K. Chu, X. Sun and Z. Ding, *J. Electroanal. Chem.*, 2023, **932**, 117220.
52 S. K. Lee, Y. Zu, A. Herrmann, Y. Geerts, K. Müllen and A. J. Bard, *J. Am. Chem. Soc.*, 1999, **121**, 3513–3520.
53 X. Qin, L. Yang, X. Wang, D. Patel, K. Chu, L. Kelland, J. Adsetts, C. Zhang, M. S. Workentin, B. Pagenkopf and Z. Ding, *ChemElectroChem*, 2022, **9**, e202200605.
54 X. Qin, L. Yang, Z. Zhan, E. Cieplechowicz, K. Chu, C. Zhang, S. Jahanghiri, G. C. Welch and Z. Ding, *Electrochim. Acta*, 2023, **450**, 142226.
55 C. Zhang, R. Zhang, R. Zhang, Q. Zhang, J.-L. Zhang and Z. Ding, *J. Inorg. Biochem.*, 2024, **254**, 112514.
56 M. Hesari and Z. Ding, *Nat. Protoc.*, 2021, **16**, 2109–2130.
57 R. Zhang, A. Zhang, M. J. Stillman and Z. Ding, *J. Phys. Chem. C*, 2020, **124**, 16568–16576.
58 K. Chu, J. R. Adsetts, Z. Whitworth, S. Kumar, E. Zysman-Colman and Z. Ding, *Langmuir*, 2023, **39**, 2829–2837.
59 A. G. Hadd, D. W. Lehmpuhl, L. R. Kuck and J. W. Birks, *J. Chem. Educ.*, 1999, **76**, 1237–1240.
60 A. Eghlimi, H. Jubaer, A. Surmiak and U. Bach, *J. Chem. Educ.*, 2019, **96**, 522–527.
61 X. Qin, Z. Zhan, R. Zhang, K. Chu, Z. Whitworth and Z. Ding, *Nanoscale*, 2023, **15**, 3864–3871.
62 X. Qin, S. Jahanghiri, Z. Zhan, K. Chu, J. Khangura and Z. Ding, *Anal. Chim. Acta*, 2024, **1285**, 342023.
63 J. Eloranta, *Experiment 3: Dynamic NMR spectroscopy*, **http://aa6kj.hopto.org/eloranta_lab/CHEM352L/experiment3.pdf**, accessed March 1, 2024.
64 J. M. Wong, R. Zhang, P. Xie, L. Yang, M. Zhang, R. Zhou, R. Wang, Y. Shen, B. Yang, H.-B. Wang and Z. Ding, *Angew. Chem., Int. Ed.*, 2020, **59**, 17461–17466.
65 T. Fujikawa, D. V. Preda, Y. Segawa, K. Itami and L. T. Scott, *Org. Lett.*, 2016, **18**, 3992–3995.